REPORT DOCUMENTATION PAGE

Form Approved OMB NO. 0704-0188

1. REPORT DATE (DD-MM-YYYY)	2. REPORT TYPE	3. DATES COVERED (From - To)
26-03-2012	Final Report	1-Oct-2008 - 31-Mar-2009

4. TITLE AND SUBTITLE

Estimating the Location and Orientation of Buried Objects Using the Magnetic Field Information of a Dipolar Response

5a. CONTRACT NUMBER

W911NF-08-1-0388

5b. GRANT NUMBER

5c. PROGRAM ELEMENT NUMBER

6. AUTHORS

Tomasz M. Grzegorczyk

5d. PROJECT NUMBER

5e. TASK NUMBER

5f. WORK UNIT NUMBER

7. PERFORMING ORGANIZATION NAMES AND ADDRESSES

Delpsi, LLC
67 Fulkerson St.

Cambridge, MA 02141 -

8. PERFORMING ORGANIZATION REPORT NUMBER

9. SPONSORING/MONITORING AGENCY NAME(S) AND ADDRESS(ES)

U.S. Army Research Office
P.O. Box 12211
Research Triangle Park, NC 27709-2211

10. SPONSOR/MONITOR'S ACRONYM(S)
ARO

11. SPONSOR/MONITOR'S REPORT NUMBER(S)
54168-EV-II.2

12. DISTRIBUTION AVAILIBILITY STATEMENT

Approved for Public Release; Distribution Unlimited

13. SUPPLEMENTARY NOTES

The views, opinions and/or findings contained in this report are those of the author(s) and should not contrued as an official Department of the Army position, policy or decision, unless so designated by other documentation.

14. ABSTRACT

Two detection approaches of unexploded ordnance (UXO) are examined, both using magnetic field data collected in the electromagnetic induction regime and using the dipole approximation as a forward model. The first approach attempts to invert for position and moment from the knowledge of the magnetic field only, from which both the vector and scalar potentials are estimated. The method, analytic in nature, avoids the necessity of solving the ill-conditioned problem typically associated with UXO detection. Although successful, the generalization of this

15. SUBJECT TERMS

Unexploded Ordnance, Electromagnetic Induction, Detection, Gauss-Newton method, Iterative method

16. SECURITY CLASSIFICATION OF:			17. LIMITATION OF ABSTRACT	15. NUMBER OF PAGES	19a. NAME OF RESPONSIBLE PERSON
a. REPORT	b. ABSTRACT	c. THIS PAGE			Thomasz Grzegorczyk
UU	UU	UU	UU		19b. TELEPHONE NUMBER 617-714-4235

Report Title

Estimating the Location and Orientation of Buried Objects Using the Magnetic Field Information of a Dipolar Response

ABSTRACT

Two detection approaches of unexploded ordnance (UXO) are examined, both using magnetic field data collected in the electromagnetic induction regime and using the dipole approximation as a forward model. The first approach attempts to invert for position and moment from the knowledge of the magnetic field only, from which both the vector and scalar potentials are estimated. The method, analytic in nature, avoids the necessity of solving the ill-conditioned problem typically associated with UXO detection. Although successful, the generalization of this method to multi-UXO is not trivial. To address the multi-target configuration, we propose an alternative method based on the Gauss-Newton iterative algorithm. The latter, more numerically involved, can be formulated with -- in principle -- an arbitrary number of targets. Initial validating results are shown here with two targets which are successfully located and identified from synthetic data with varying degrees of noise.

Enter List of papers submitted or published that acknowledge ARO support from the start of the project to the date of this printing. List the papers, including journal references, in the following categories:

(a) Papers published in peer-reviewed journals (N/A for none)

Received Paper

TOTAL:

Number of Papers published in peer-reviewed journals:

(b) Papers published in non-peer-reviewed journals (N/A for none)

Received Paper

TOTAL:

Number of Papers published in non peer-reviewed journals:

(c) Presentations

Results were part of a presentation at the 2009 SERDP Symposium

Number of Presentations: 1.00

Non Peer-Reviewed Conference Proceeding publications (other than abstracts):

Received Paper

TOTAL:

Number of Non Peer-Reviewed Conference Proceeding publications (other than abstracts):

Peer-Reviewed Conference Proceeding publications (other than abstracts):

Received	Paper
2012/03/26 1(1	Tomasz M. Grzegorczyk, Benjamin Barrowes, Fridon Shubitidze, J. P. Fernandez, Irma Shamatava, Kevin ONeill. Detection of multiple subsurface metallic targets using EMI data, Detection and Sensing of Mines, Explosive Objects, and Obscured Targets XIV. , Orlando, FL, USA. : ,

TOTAL: **1**

Number of Peer-Reviewed Conference Proceeding publications (other than abstracts):

(d) Manuscripts

Received	Paper

TOTAL:

Number of Manuscripts:

Books

Received	Paper

TOTAL:

Patents Submitted

Patents Awarded

Awards

Graduate Students

NAME	PERCENT_SUPPORTED
FTE Equivalent:	
Total Number:	

Names of Post Doctorates

NAME	PERCENT_SUPPORTED
FTE Equivalent:	
Total Number:	

Names of Faculty Supported

NAME	PERCENT_SUPPORTED
FTE Equivalent:	
Total Number:	

Names of Under Graduate students supported

NAME	PERCENT SUPPORTED
FTE Equivalent:	
Total Number:	

Student Metrics

This section only applies to graduating undergraduates supported by this agreement in this reporting period

The number of undergraduates funded by this agreement who graduated during this period:	0.00
The number of undergraduates funded by this agreement who graduated during this period with a degree in science, mathematics, engineering, or technology fields:.....	0.00
The number of undergraduates funded by your agreement who graduated during this period and will continue to pursue a graduate or Ph.D. degree in science, mathematics, engineering, or technology fields:.....	0.00
Number of graduating undergraduates who achieved a 3.5 GPA to 4.0 (4.0 max scale):	0.00
Number of graduating undergraduates funded by a DoD funded Center of Excellence grant for Education, Research and Engineering:	0.00
The number of undergraduates funded by your agreement who graduated during this period and intend to work for the Department of Defense	0.00
The number of undergraduates funded by your agreement who graduated during this period and will receive scholarships or fellowships for further studies in science, mathematics, engineering or technology fields:	0.00

Names of Personnel receiving masters degrees

NAME
Total Number:

Names of personnel receiving PHDs

NAME
Total Number:

Names of other research staff

NAME	PERCENT SUPPORTED
Tomasz M Grzegorczyk	0.33
FTE Equivalent:	**0.33**
Total Number:	**1**

Sub Contractors (DD882)

Inventions (DD882)

Scientific Progress

Please see report

Technology Transfer

Delpsi, LLC – 81 Church Street (Unit 2), Newton, MA 02458-2088
Tel: 617 467 5561 – http://www.delpsi.com

Estimating the Location and Orientation of Buried Objects Using the Magnetic Field Information of a Dipolar Response

Contract #W911NF-08-1-0388

Tomasz M. Grzegorczyk

March 31, 2009

Final Report

Submitted to : Army Research Office

Person of contact : Dr. Tomasz M. Grzegorczyk
Email : tomasz.grzegorczyk@delpsi.com
Tel/Fax : 617-467 5561

Contents

1 Statement of the problem studied

The detection and discrimination of unexploded ordnances (UXO) is a challenging task which requires sophisticated forward models and efficient inversion algorithms. Due to the large number of unknowns (target's size, composition, position, orientation, and number), the latter often do not solve the entire non-linear problem at once. Instead, specific but optimized techniques are typically developed for the inversion of a subset of parameters, and are used in conjunction with one another.

Although the determination of the target's size and composition usually requires advances mathematical models – which have been the subject of some of our previous work – the determination of the position and orientation is more tolerant to some approximations and hence, can be performed in a simpler manner. Typically, an optimization approach is often used, whereby the measured magnetic field is matched to the one produced by a forward model, in which the unknown coefficients are solved for by a matrix inversion. This approach, however, can produce an ill-posed inverse scattering problem when applied to the inversion of the location and orientation of the object.

Recently, an alternative method to accomplish this inversion without having to solve an ill-posed problem has been proposed. The method assumes that the secondary field induced by the buried target is akin to that of three orthogonal dipoles, whose locations and moments are obtained analytically from the estimation of the magnetic vector potential and the electric scalar potential, in addition to the measured magnetic field. These potentials are computed via the intermediate step of introducing surface magnetic dipoles over a fictitious boundary, whose amplitudes are determined by matching the magnetic fields, and relating these dipoles to the potential via well known relations. Once the three quantities are known, the distance vector, the eigenvalues of the polarizability tensor, and the Euler angles are obtained by a simple and well-behaved matrix inversion.

Following this approach, we investigate the robustness of this new method to various amounts of noise in the measured magnetic field as well as the influence of various numerical parameters on the accuracy of the estimated position and dipole moment.

The major drawback of the previous approach, however, is that it cannot be generalized to multiple targets (at the time of this writing). Yet, multiple targets are often encountered in the field, with UXO buried alongside other UXO or alongside clutter items. It is therefore important to devise an analysis method flexible enough to address these more challenging situations as well. With this purpose in mind, we propose and formulate an inversion algorithm based on an iterative Gauss-Newton method, for which the number of targets is in principle unlimited. Initial implementation and validation of the method are presented.

2 Summary of the most important results

2.1 $(\bar{H},\bar{A},\psi)$ method to estimate an object location, orientation, and dipole moment

2.1.1 Background and procedure

Our past efforts have focused on developing some of the most up-to-date forward and inverse algorithms for the modeling of UXO in the electromagnetic induction (EMI) regime, in both the frequency domain and the time domain. These include the use of the spheroidal system for the general modeling of axially symmetric UXO [1–3] (a more general model than the dipole model [4, 5]). the use of analytical metrics for the characterization of UXO [6], the use of learning algorithms for their discrimination [7], and the recent generalization of our modeling capabilities to the ellipsoidal coordinate system [8].

Although the detection of UXO is relatively simple, their discrimination is a vastly more complex task. Treating as unknowns the location, orientation, and composition of the object produces highly non-linear problems which are both challenging and time-consuming to solve. Effectively, the forward algorithms mentioned previously become drastically more efficient if some unknowns can be determined by add-on methods. Based on a dipole approximation, an analytical method has been recently proposed for the inversion of the location and strength of the dipoles, effectively providing information on the location and orientation of the target in the ground [9]. The method is based on the near-field approximation of a magnetic dipole, for which the field and the two potentials are given by [10]:

$$\bar{H} = \frac{e^{\mathrm{i}kR}}{4\pi R^3}\left[\left(\frac{3\bar{R}(\bar{R}\cdot\bar{m})}{R^2}-\bar{m}\right)(1-\mathrm{i}kR)-k^2\bar{R}\times(\bar{R}\times\bar{m})\right], \tag{1a}$$

$$\bar{A} = \mu_0\frac{\bar{m}\times\bar{R}}{4\pi R^3}(1-\mathrm{i}kR)e^{\mathrm{i}kR}, \tag{1b}$$

$$\psi = \frac{\bar{R}\cdot\bar{m}}{4\pi R^3}(1-\mathrm{i}kR)e^{\mathrm{i}kR}, \tag{1c}$$

where $\bar{R}=\bar{r}-\bar{r}'$, $\bar{r}$ and $\bar{r}'$ being the position of the observation and of the source, respectively. Note that we have not made any assumptions as to which term could potentially be neglected, but certainly some terms can be, given that we work in the limit of $k\to 0$. Typically, the k^2 term in Eq. (1a) can be neglected, as well as $(1-\mathrm{i}kR)\exp(\mathrm{i}kR)$, which leaves a problem independent of k, *i.e.* independent of frequency.

These equations can be inverted to yield $\bar{R}$ and $\bar{m}$ as function of $\bar{H}$, $\bar{A}$, and ψ, and yield:

$$\bar{R} = \frac{2\bar{H}\psi+(\bar{H}\times\bar{A}/\mu_0)}{|\bar{H}|^2}, \tag{2a}$$

$$\bar{m} = \frac{R}{G(R)}\left(\bar{R}\psi-\left(\bar{A}/\mu_0\times\bar{R}\right)\right) \tag{2b}$$

where

$$G(R) = \frac{e^{\mathrm{i}kR}}{4\pi}(1-\mathrm{i}kR)\simeq\frac{1}{4\pi}. \tag{3}$$

The whole purpose is therefore to estimate $\bar{A}$ and ψ knowing only the magnetic field $\bar{H}$ over a measurement grid.

2.1.2 Determining $\bar{R}$

Following [9], we use a fictitious surface of magnetic dipoles defined by

$$\bar{m}(\bar{r}') = \hat{x}\sum_{n=1}^{N} P_n^x F_n^x(\bar{r}') + \hat{y}\sum_{n=1}^{N} P_n^y F_n^y(\bar{r}') + \hat{z}\sum_{n=1}^{N} P_n^z F_n^z(\bar{r}'). \tag{4}$$

The functions $F_n^{x,y,z}$ are basis functions whereas the unknown coefficients $P_n^{x,y,z}$ are determined by matching the measured (known) vectorial magnetic field over a reference grid. Starting from Eq. (21) in [9], we write the magnetic field as

$$\bar{H}(\bar{r}) = \sum_{n=1}^{N} P_n^x \bar{f}^x(\bar{r}-\bar{r}'_n) + \sum_{n=1}^{N} P_n^y \bar{f}^y(\bar{r}-\bar{r}'_n) + \sum_{n=1}^{N} P_n^z \bar{f}^z(\bar{r}-\bar{r}'_n) \tag{5}$$

where

$$\bar{f}^\eta(\bar{r}-\bar{r}'_n) = \int_{S_n} \mathrm{d}S \left(3(\bar{r}-\bar{r}'_n)\left[(\bar{r}-\bar{r}'_n)\cdot\hat{\eta}\right] - |\bar{r}-\bar{r}'_n|^2\hat{\eta}\right)\frac{G(|\bar{r}-\bar{r}'_n|)}{|\bar{r}-\bar{r}'_n|^5}, \tag{6}$$

and where $\hat{\eta} = \hat{x}, \hat{y}, \hat{z}$ and S_n refers to the discretization of the fictitious surface. From Eq. (5), the $\hat{x}$ component of the magnetic field is given by:

$$\begin{aligned}\hat{x}\cdot\bar{H}(\bar{r}) = H_x(\bar{r}) = \sum_{n=1}^{N} P_n^x \hat{x}\cdot\bar{f}^x(\bar{r}-\bar{r}'_n) + \sum_{n=1}^{N} P_n^y \hat{x}\cdot\bar{f}^y(\bar{r}-\bar{r}'_n) \\ + \sum_{n=1}^{N} P_n^z \hat{x}\cdot\bar{f}^z(\bar{r}-\bar{r}'_n).\end{aligned} \tag{7}$$

Evaluating this equation over P observation points (typically over the measurement grid):

$$\begin{aligned}\begin{bmatrix} H_x(\bar{r}_1) \\ H_x(\bar{r}_2) \\ \vdots \\ H_x(\bar{r}_P)\end{bmatrix} &= \begin{bmatrix} \hat{x}\cdot\bar{f}^x(\bar{r}_1-\bar{r}'_1) & \hat{x}\cdot\bar{f}^x(\bar{r}_1-\bar{r}'_2) & \dots & \hat{x}\cdot\bar{f}^x(\bar{r}_1-\bar{r}'_N) \\ \hat{x}\cdot\bar{f}^x(\bar{r}_2-\bar{r}'_1) & \hat{x}\cdot\bar{f}^x(\bar{r}_2-\bar{r}'_2) & \dots & \hat{x}\cdot\bar{f}^x(\bar{r}_2-\bar{r}'_N) \\ \vdots & \vdots & \ddots & \vdots \\ \hat{x}\cdot\bar{f}^x(\bar{r}_P-\bar{r}'_1) & \hat{x}\cdot\bar{f}^x(\bar{r}_P-\bar{r}'_2) & \dots & \hat{x}\cdot\bar{f}^x(\bar{r}_P-\bar{r}'_N)\end{bmatrix}\cdot\begin{bmatrix} P_1^x \\ P_2^x \\ \vdots \\ P_N^x\end{bmatrix} \\ &+ \begin{bmatrix} \hat{x}\cdot\bar{f}^y(\bar{r}_1-\bar{r}'_1) & \hat{x}\cdot\bar{f}^y(\bar{r}_1-\bar{r}'_2) & \dots & \hat{x}\cdot\bar{f}^y(\bar{r}_1-\bar{r}'_N) \\ \hat{x}\cdot\bar{f}^y(\bar{r}_2-\bar{r}'_1) & \hat{x}\cdot\bar{f}^y(\bar{r}_2-\bar{r}'_2) & \dots & \hat{x}\cdot\bar{f}^y(\bar{r}_2-\bar{r}'_N) \\ \vdots & \vdots & \ddots & \vdots \\ \hat{x}\cdot\bar{f}^y(\bar{r}_P-\bar{r}'_1) & \hat{x}\cdot\bar{f}^y(\bar{r}_P-\bar{r}'_2) & \dots & \hat{x}\cdot\bar{f}^y(\bar{r}_P-\bar{r}'_N)\end{bmatrix}\cdot\begin{bmatrix} P_1^y \\ P_2^y \\ \vdots \\ P_N^y\end{bmatrix} \\ &+ \begin{bmatrix} \hat{x}\cdot\bar{f}^z(\bar{r}_1-\bar{r}'_1) & \hat{x}\cdot\bar{f}^z(\bar{r}_1-\bar{r}'_2) & \dots & \hat{x}\cdot\bar{f}^z(\bar{r}_1-\bar{r}'_N) \\ \hat{x}\cdot\bar{f}^z(\bar{r}_2-\bar{r}'_1) & \hat{x}\cdot\bar{f}^z(\bar{r}_2-\bar{r}'_2) & \dots & \hat{x}\cdot\bar{f}^z(\bar{r}_2-\bar{r}'_N) \\ \vdots & \vdots & \ddots & \vdots \\ \hat{x}\cdot\bar{f}^z(\bar{r}_P-\bar{r}'_1) & \hat{x}\cdot\bar{f}^z(\bar{r}_P-\bar{r}'_2) & \dots & \hat{x}\cdot\bar{f}^z(\bar{r}_P-\bar{r}'_N)\end{bmatrix}\cdot\begin{bmatrix} P_1^z \\ P_2^z \\ \vdots \\ P_N^z\end{bmatrix}\end{aligned} \tag{8}$$

This equation is rewritten in matrix form as

$$\bar{H}_x = \bar{\bar{F}}_{xx}\cdot\bar{P}^x + \bar{\bar{F}}_{yx}\cdot\bar{P}^y + \bar{\bar{F}}_{zx}\cdot\bar{P}^z. \tag{9a}$$

Similar equations can be written for $\bar{H}_y$ and $\bar{H}_z$:

$$\bar{H}_y = \bar{\bar{F}}_{xy}\cdot\bar{P}^x + \bar{\bar{F}}_{yy}\cdot\bar{P}^y + \bar{\bar{F}}_{zy}\cdot\bar{P}^z, \tag{9b}$$

$$\bar{H}_z = \bar{\bar{F}}_{xz}\cdot\bar{P}^x + \bar{\bar{F}}_{yz}\cdot\bar{P}^y + \bar{\bar{F}}_{zz}\cdot\bar{P}^z. \tag{9c}$$

Real dipole moments	:	$\bar{m}$ =(1,0,2)
Real dipole position	:	(x,y,z)=(10 cm,−2 cm,−45 cm)
Fictitious surface	:	$z' = -30$ cm
Measurement grid	:	8×8 points over $[-50,50]$ cm×$[-50,50]$ cm
Fictitious grid	:	8×8 points over $[-50,50]$ cm×$[-50,50]$ cm

Table 1: Definition of the reference parameters.

The system can eventually be gathered in a matrix form as

$$\begin{bmatrix}\bar{H}_x\\ \bar{H}_y\\ \bar{H}_z\end{bmatrix} = \begin{bmatrix}\bar{\bar{F}}_{xx} & \bar{\bar{F}}_{yx} & \bar{\bar{F}}_{zx}\\ \bar{\bar{F}}_{xy} & \bar{\bar{F}}_{yy} & \bar{\bar{F}}_{zy}\\ \bar{\bar{F}}_{xz} & \bar{\bar{F}}_{yz} & \bar{\bar{F}}_{zz}\end{bmatrix}\cdot\begin{bmatrix}\bar{P}^x\\ \bar{P}^y\\ \bar{P}^z\end{bmatrix}, \tag{10}$$

or

$$\bar{H} = \bar{\bar{F}}\cdot\bar{P}, \tag{11}$$

from which $\bar{P}$ can be obtained, typically as a least square solution:

$$\bar{P} = \left(\bar{\bar{F}}^T\cdot\bar{\bar{F}}\right)^{-1}\cdot\left(\bar{\bar{F}}^T\cdot\bar{H}\right). \tag{12}$$

Once these coefficients are obtained, the dipole moments over the fictitious surface are obtained from Eq. (4), from which $(\bar{H},\bar{A},\psi)$ are obtained via Eqs. (1), from which the position of the dipole is obtained via Eq. (2a).

For the numerical illustration of the method, the parameters of Table 1 are used, unless specified otherwise. The variations in the retrieved positions due to other parameters is illustrated subsequently. Note that in the subsequent results, we plot $\bar{r}' = \bar{r} - \bar{R}$. In addition, the captions of the figures list the values of the root mean square errors (rmse) of $\bar{H}$,

$$\rho_{H_\eta} = \sqrt{\frac{1}{P}\sum_{i=1}^{P}\left(H_\eta^{mea} - H_\eta^{comp}\right)^2}, \quad \eta = x,y,z \tag{13a}$$

$$\bar{\rho}_H = (\rho_{H_x},\rho_{H_y},\rho_{H_z}), \tag{13b}$$

and similarly for $\bar{A}$ and for the one value of V. The root mean square errors give some sense as to what components are well or poorly estimated, and their influence on the position estimation. Typically, the magnetic field rmse should be very low (less than 10^{-4} since it is the field used to derive the unknown coefficients*), whereas the vector and scalar magnetic potentials should have an rmse of 10^{-2} or less.

The first result, which can be used as a reference, is shown in Fig. 1, and illustrates the fact that the retrieval of $\bar{R}$ is not trivial. In particular, important oscillations are seen in the retrieved components. Nonetheless, the average values are relatively reasonable, and the variances are between 1 cm and 2 cm, which would be acceptable in a field measurement. The influence of other parameters such as the position of the fictitious surface, the size of the measurement grid, the size of the fictitious grid, or the use of some components of the magnetic field only are all illustrated in Figs. 2-6.

*Note that this order of magnitude does not necessarily hold when only few components of the magnetic field are used.

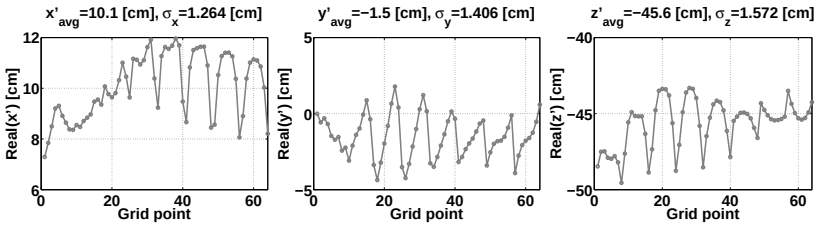

Figure 1: Retrieved position for the parameters of Table 1. The amplitudes of the oscillations are quite large but the variances are reasonable (compared to the field precision required). The average values are relatively close to the expected ones. $\bar{\rho}_H$ =(1.3,1.1,1.7)×10^{-9}, $\bar{\rho}_A$ =(1.4,2.5,2.7)×10^{-2}, ρ_V =5×10^{-3}.

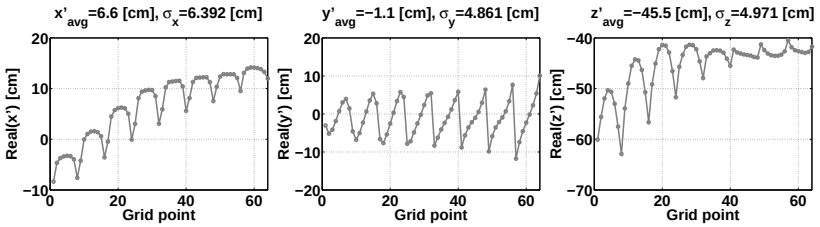

(a) $z' = -20$ cm: Overall the estimation of the location is worse, with increased oscillations in all the components (reflected also by larger variances). $\bar{\rho}_H$ =(0.94,0.60,1.06)×10^{-12}, $\bar{\rho}_A$ =(1.5,2.9,3.0)×10^{-2}, ρ_V =3.3×10^{-2}.

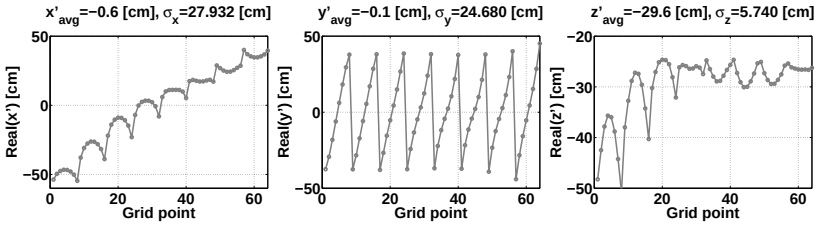

(b) $z' = -10$ cm: The estimates become significantly worse. It is probably due to the fact that being so far from the real source, the fictitious dipoles do not capture the original field very well. Increasing the size of the fictitious surface and the number of fictitious dipoles seems to improve the results (see Fig. 5). $\bar{\rho}_H$ =(5.19,3.76,5.04)×10^{-15}, $\bar{\rho}_A$ =(0.59,1.24,0.66)×10^{-1}, ρ_V =1.79×10^{-1}.

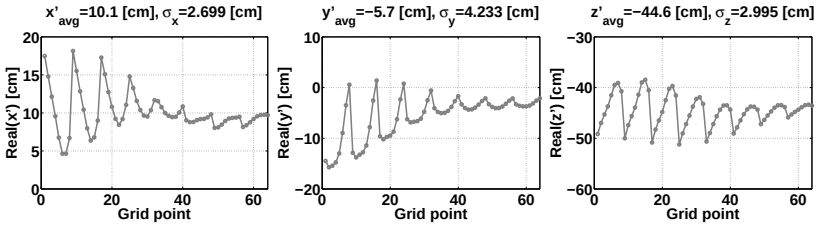

(c) $z' = -44$ cm: The estimate is relatively good, except in y'. The good results are probably due to the proximity of the fictitious source to the real source, thus capturing most of the radiated field. $\bar{\rho}_H$ =(3.73,2.27,4.36)×10^{-5}, $\bar{\rho}_A$ =(3.6,2.6,4.7)×10^{-2}, ρ_V =2.16e-04.

Figure 2: Varying the position of the fictitious surface z'.

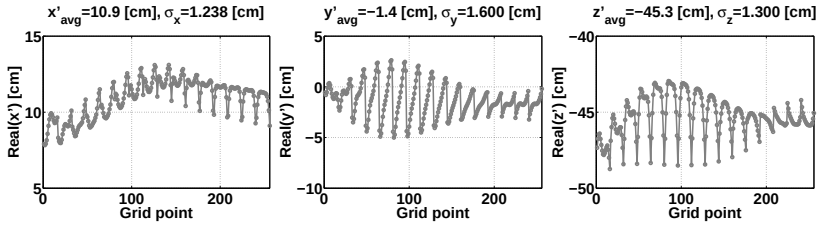

(a) 16×16 points over [-50,50] cm×[-50,50] cm: The results are relatively similar to the reference Fig. 1. $\bar{\rho}_H$ =(4.39,3.83,5.05)×10^{-4}, $\bar{\rho}_A$ =(1.7,2.7,3.3)×10^{-2}, ρ_V =4×10^{-3}.

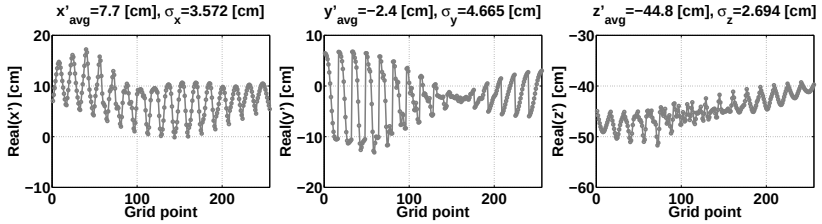

(b) 16×16 points over [-100,100] cm×[-100,100] cm: Increasing the size of the measurement grid does not necessarily improves the results. Most likely the fictitious grid has to be adjusted as well. $\bar{\rho}_H$ =(0.9,0.8,1.4)×10^{-3}, $\bar{\rho}_A$ =(0.9,1.2,1.6)×10^{-2}, ρ_V =1×10^{-3}.

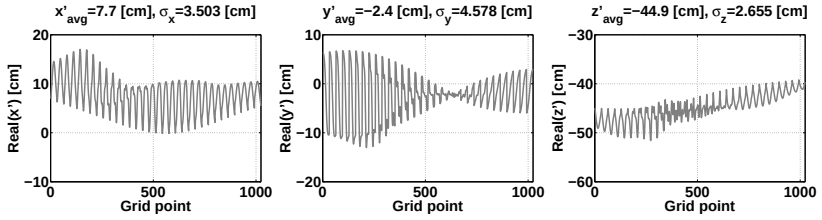

(c) 32×32 points over [-100,100] cm×[-100,100] cm: Same conclusion as the previous case (note that a difference inversion scheme has been used, because of computation time). $\bar{\rho}_H$ =(1.0,0.8,1.3)×10^{-3}, $\bar{\rho}_A$ =(0.9,1.3,1.6)×10^{-2}, ρ_V =1×10^{-3}.

Figure 3: Varying the size of the measurement grid.

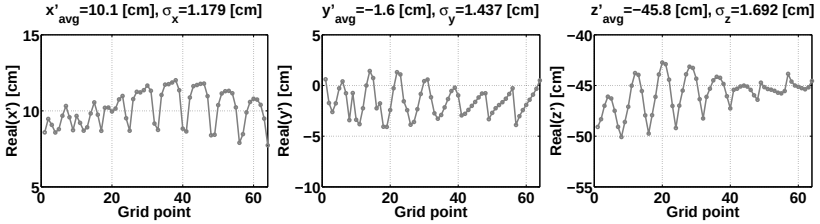

(a) 16×16 points over [-50,50] cm×[-50,50] cm: Somewhat similar results to the reference Fig. 1. $\bar{\rho}_H$ =(5.19,5.48,7.61)$\times 10^{-10}$, $\bar{\rho}_A$ =(1.4,2.7,2.9)$\times 10^{-2}$, ρ_V =4×10^{-3}.

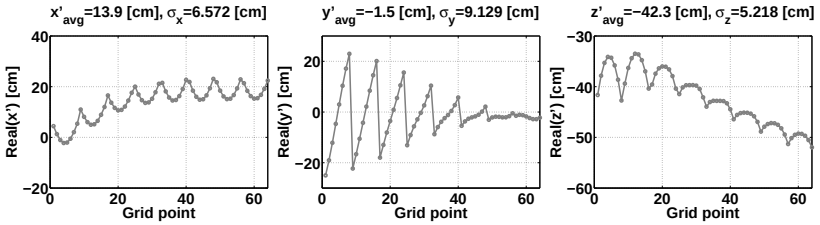

(b) 16×16 points over [-100,100] cm×[-100,100] cm: The results are degraded (essentially seen in the larger variances). Probably due to a well over-determined system. $\bar{\rho}_H$ =(4.04,4.66,6.16)$\times 10^{-10}$, $\bar{\rho}_A$ =(3.0,7.8,8.4)$\times 10^{-2}$, ρ_V =9×10^{-3}.

Figure 4: Varying the size of the fictitious grid.

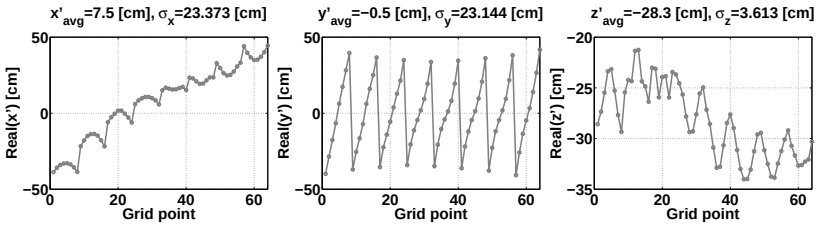

Figure 5: Increased fictitious grid when further away from the real source: the results are improved compared to Fig. 2(b). $\bar{\rho}_H$ =(8.33,5.57,8.98)$\times 10^{-16}$, $\bar{\rho}_A$ =(0.50,1.65,0.95)$\times 10^{-1}$, ρ_V =1.43×10^{-1}.

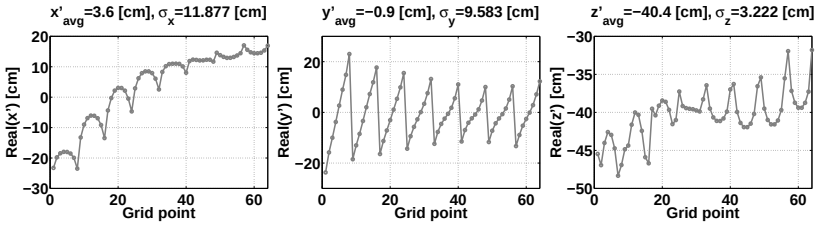

(a) Using only (H_x, H_y) (thus a sub-system of Eq. (10)). The results are significantly degraded. $\bar{\rho}_H$ =(0,0,8.15)×10^{-2}, $\bar{\rho}_A$ =(1.8,2.8,2.9)×10^{-2}, ρ_V =6.9×10^{-2}.

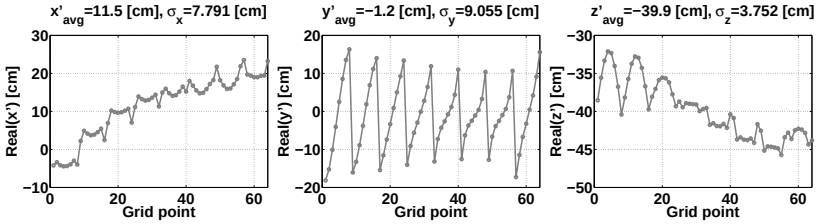

(b) Using only H_z (thus a sub-system of Eq. (10)). The results are better than using only (H_x, H_y), suggesting that standard GEM-3 measurements might be reasonably usable. $\bar{\rho}_H$ =(4.5,2.1,0)×10^{-2}, $\bar{\rho}_A$ =(2.6,8.9,6.9)×10^{-2}, ρ_V =3.1×10^{-1}.

Figure 6: Using only some components of the magnetic field.

2.1.3 Determining $\bar{m}$

The average dipole moments are determined from Eq. (2b) using the estimated positions and potentials. The results are summarized in Table 2, along with those for the average $\bar{R}$, for the same case as in the previous section. The table illustrates the influence of various parameters on the accuracy of the inverted results, in particular the size of the measurement grid, the side of the fictitious grid, and the number of components of the magnetic field used in the inversion.

2.1.4 Using GA to determine $\bar{R}$ and m

The encouraging results of the previous section prove that Eqs. (2) and the use of a fictitious boundary for unknown 3D dipoles provide a good way to estimate the location and moments of a dipole knowing only the magnetic field over an observation grid. In real life, however, results cannot be compared against a known truth like previously, where the exact position of the dipole is known. Hence, another metric needs to be chosen.

In what follows, we use the standard deviation in the estimate of $\bar{R}$ (*i.e.* σ_{xyz} in the previous results) as a metric, supposing that the smaller it is, the more accurate the estimate. This is somewhat intuitive because we expect the mean to be more trustworthy if the data are more concentrated around it.[†] This metric, which exact formulation is examined subsequently, provides a measure of goodness so that we can minimize it using some stochastic methods. We have implemented here a Genetic Algorithm (GA) for that purpose, using 5 unknown parameters:

(*i*) The starting coordinate x_{min} of the observation grid in x, within the bounds -60 cm and -40 cm. We suppose that the observation and fictitious grid overlap in the (xy) plane and are only different by their z position.

(*ii*) The starting coordinate y_{min} of the observation grid in y, with the same assumptions and same bounds. In addition, we suppose the grid to be 1 m$\times$1 m so that the first two parameters totally define the observation and fictitious grids in the (xy) plane as $[x_{min}, x_{min}+1\text{ m}]$, $[y_{min}, y_{min}+1\text{ m}]$.

(*iii*) The vertical position of the fictitious grid, within -50 cm and -10 cm.

(*iv*) The number of measurement points N_o on the observation grid (same in x and y).

(*v*) The number of dipoles N_d on the fictitious grid (same in x and y).

The other GA parameters are a population size of 100, a probability of crossover of 60%, a probability of mutation of 5%, and 20 iterations. The choice of the metric is likely to change the estimates of $\bar{R}$ and $\bar{m}$, so that we examine this effect in Table 3. For example, if the metric is chosen to be only σ_z, the fitness of the reference result is 1.572×10^{-2}, as shown in Fig. 1.

The results again show the influence of various parameters on the accuracy of the results. In particular, the measured dataset (all components of the magnetic field or only its $\hat{z}$ component) are seen to have an important impact on result accuracy. It is expected that the new generation of EMI sensors will be able to measured full vectorial magnetic fields with multiple primary incidences, which should improve field-based inversion results significantly.

[†]Note that this assumes that the estimator is unbiased, which we expect to be since Eq. (2a) is an exact relation.

Case	x [cm]	y [cm]	z' [cm]	m_x	m_y	m_z	Figure
True value	10	−2	−45	1	0	2	
Reference	10.1	−1.1	−45.5	0.99	−0.02	1.95	1
Varying the position of the fictitious surface z'							
$z' = -20$ cm	6.6	−1.1	−45.5	0.94	−0.04	1.54	2(a)
$z' = -10$ cm	−0.6	−0.1	−29.6	0.13	−0.009	0.21	2(b)
$z' = -44$ cm	10.1	−5.7	−44.6	0.97	0.19	1.97	2(c)
Varying the size of the measurement grid							
16×16 points over $[-50, 50]$ cm$\times[-50, 50]$ cm	10.9	−1.4	−45.3	0.92	−0.03	1.95	3(a)
16×16 points over $[-100, 100]$ cm$\times[-100, 100]$ cm	7.7	−2.4	−44.8	1.18	0.001	2.04	3(b)
32×32 points over $[-100, 100]$ cm$\times[-100, 100]$ cm	7.7	−2.4	−44.9	1.19	0.002	2.05	3(c)
Varying the size of the fictitious grid							
16×16 points over $[-50, 50]$ cm$\times[-50, 50]$ cm	10.1	−1.6	−45.8	1.01	−0.02	1.98	4(a)
16×16 points over $[-100, 100]$ cm$\times[-100, 100]$ cm	13.9	−1.5	−42.3	0.34	−0.01	1.69	4(b)
Using only some components of the magnetic field							
Using only (H_x, H_y)	3.6	−0.9	−40.4	0.70	−0.03	1.08	6(a)
Using only H_z	11.5	−1.2	−39.9	0.31	−0.02	1.37	6(b)

Table 2: Retrieved average positions and moments for the cases in Section 2.1.2.

metric	N_o	N_d	x_{min} [cm]	y_{min} [cm]	z_{fic} [cm]	$\bar{R}$ [cm]	$\bar{m}$	fitness $\times 10^{-2}$
Measuring (H_x, H_y, H_z)								
σ_z	8	8	−50	−45	−39	(10.8, −1.6, −45.0)	(0.94,0.006,1.99)	0.84
σ_x	9	9	−44	−51	−36	(10.7, −1.97, −45.0)	(0.95,0.002,1.99)	0.84
$(\sigma_x+\sigma_y+\sigma_z)/3$	9	9	−42	−52	−39	(10.4, −2.01, −45.0)	(0.97,0,2)	0.57
$\max(\sigma_x,\sigma_y,\sigma_z)$	9	9	−40	−49	−38	(10.3, −1.95, −45.0)	(0.97,0.003,1.99)	0.88
Measuring H_z								
σ_z	9	9	−59	−54	−34	(9.18, −2.5, −42.3)	(0.56,0.01,1.5)	2.31
σ_x	10	9	−42	−52	−47	(11.4, −1.98, −46.2)†	(0.93, −0.002,2.06)	1.68
$(\sigma_x+\sigma_y+\sigma_z)/3$	10	9	−48	−51	−47.5	(11.08, −2.23, −46.4)‡	(0.97,0.02,1.97)	2.53
$\max(\sigma_x,\sigma_y,\sigma_z)$	9	10	−58	−51	−42.2	(10.2, −1.72, −45.91)	(0.88, −0.02,1.87)	3.31

Table 3: GA results for various metrics.

† Since the fictitious surface is below the estimated source depth, this case is re-evaluated by forcing the fictitious surface at −46.2 cm, to yield the new parameters: $\bar{R} = (11.93, -1.98, -45.7)$ cm, $\bar{m} = (0.84, 0.002, 2.02)$, fitness=$1.8\times10^{-2}$.

‡ We proceed in the same way as in †, to obtain: $\bar{R} = (11.6, -2.17, -45.5)$ cm, $\bar{m} = (0.83, 0.002, 1.92)$, fitness=$2.54\times10^{-2}$.

2.2 Detection of two targets using a Newton based method

2.2.1 Motivation

Although the previous $(\bar{H},\bar{A},\psi)$ method has been shown to yield reasonable position and dipole moment estimates, we have found that its major drawback is that it is not straightforward to generalize to a multi-target configuration, whereby multiple dipoles (position and dipole moments) need to be inverted for. Yet, multiple targets are often encountered in the field, with UXO buried alongside other UXO or alongside clutter items.

In the remainder of this report, we propose and formulate an alternative method to address this issue. The method is based on an iterative Gauss-Newton implementation which, in principle, does not limit the number of unknowns and hence, can potentially invert for multiple positions and dipole moments simultaneously. As we show subsequently, the Jacobian matrices required by the method take analytical forms within a dipole approximation, which we therefore follow in order to enhance the efficacy of the method. Initial results on two-target inversion are shown to be encouraging.

We assume a bistatic configuration were two targets are buried at positions $\bar{r}'_1$ and $\bar{r}'_2$ and respond with a single dipole moment each, denoted by $\bar{m}_1$ and $\bar{m}_2$, respectively. The purpose is to use the measured components of the magnetic field to invert for $(\bar{r}'_1,\bar{m}_1)$ and $(\bar{r}'_2,\bar{m}_2)$.

The magnetic field is given by

$$\bar{H} = \frac{1}{R^3}\left[\frac{3\bar{R}(\bar{R}\cdot\bar{m})}{R^2} - \bar{m}\right] \tag{14}$$

where $\bar{R} = \bar{r} - \bar{r}' = \hat{x}(x-x') + \hat{y}(y-y') + \hat{z}(z-z')$ (the prime coordinates corresponding to the source and the unprimed to the observation) and $\bar{m} = \hat{x}m_x + \hat{y}m_y + \hat{z}m_z$. In the case of two targets,

$$\bar{H} = \bar{H}_1 + \bar{H}_2 \tag{15}$$

where $\bar{H}_1$ and $\bar{H}_2$ are generated by the two targets respectively, and each obeying Eq. (14).

In the bistatic case, the dipole $\bar{m}$ in Eq. (14) represents the only source in the system: it is buried at a position $\bar{R}$ and produces the magnetic field that is measured by the sensor across the observation grid. In the monostatic case, however, the dipole moment depends on the polarizability of the target and on the primary field at its location, which is written as

$$\bar{m} = \bar{\bar{M}}\cdot\bar{H}^{pr}, \tag{16}$$

where $\bar{\bar{M}}$ is the polarizability tensor and $\bar{H}^{pr}$ is the primary field at the target locations. In the monostatic configuration, the sensor emits and receives at each point on the observation grid. At each point, the primary field at the location of the target $\bar{H}^{pr}$ needs to be computed and is used to weight the polarizability tensor $\bar{\bar{M}}$. This means that the dipole moment $\bar{m}$ is different for each location of the sensor. However, the polarizability $\bar{\bar{M}}$ is constant and needs to be inverted for, later to be used as a classification metric between different UXO.

2.2.2 Newton method

In this section, the formulation of the Gauss-Newton algorithm is presented for both monostatic and bistatic configurations, as well as when all the components of the magnetic field are measured or when only H_z is measured.

Bistatic case: Using only the measured H_z

The master equation on which the iterative scheme is based is the standard normal equation written as

$$\bar{\bar{J}}_z^T \cdot \bar{\bar{J}}_z \cdot \Delta\bar{\mathrm{x}} = \bar{\bar{J}}_z^T \cdot \left(H_z^{mea} - H_z^{comp}\right) \tag{17}$$

where $\bar{\mathrm{x}}$ is the unknown vector of dimensions $[M \times 1]$, $\Delta\bar{\mathrm{x}} = \bar{\mathrm{x}}^{i+1} - \bar{\mathrm{x}}^i$ is the unknown and provides the updated quantities of $\bar{\mathrm{x}}$ at each iteration, $\bar{\bar{J}}_z$ is the Jacobian matrix of dimensions $[N \times M]$, H_z^{mea} and H_z^{comp} are the measured and computed z components of the magnetic field, respectively, of dimensions $[N \times 1]$.

In the two target detection case, we need to iterate for two positions and two momenta so that

$$\bar{\mathrm{x}} = [X_1, Y_1, Z_1, X_2, Y_2, Z_2, m_{x1}, m_{y1}, m_{z1}, m_{x2}, m_{y2}, m_{z2}] \tag{18}$$

where $X_1 = x - x_1'$, and similarly for the other components. Therefore in this case, $M = 12$. Explicitely, the Jacobian matrix is

$$\bar{\bar{J}}_z = \left[\bar{\bar{J}}_{z_{\bar{R}_1}}\ \bar{\bar{J}}_{z_{\bar{R}_2}}\ \bar{\bar{J}}_{z_{\bar{m}_1}}\ \bar{\bar{J}}_{z_{\bar{m}_2}}\right] \tag{19a}$$

$$\bar{\bar{J}}_{z_{\bar{R}_i}} = \begin{pmatrix} \frac{\partial H_z^{(1)}}{\partial X_i} & \frac{\partial H_z^{(1)}}{\partial Y_i} & \frac{\partial H_z^{(1)}}{\partial Z_i} \\ \frac{\partial H_z^{(2)}}{\partial X_i} & \frac{\partial H_z^{(2)}}{\partial Y_i} & \frac{\partial H_z^{(2)}}{\partial Z_i} \\ \vdots & \ddots & \vdots \\ \frac{\partial H_z^{(N)}}{\partial X_i} & \frac{\partial H_z^{(N)}}{\partial Y_i} & \frac{\partial H_z^{(N)}}{\partial Z_i} \end{pmatrix}, \quad \bar{\bar{J}}_{z_{\bar{m}_i}} = \begin{pmatrix} \frac{\partial H_z^{(1)}}{\partial m_{x_i}} & \frac{\partial H_z^{(1)}}{\partial m_{y_i}} & \frac{\partial H_z^{(1)}}{\partial m_{z_i}} \\ \frac{\partial H_z^{(2)}}{\partial m_{x_i}} & \frac{\partial H_z^{(2)}}{\partial m_{y_i}} & \frac{\partial H_z^{(2)}}{\partial m_{z_i}} \\ \vdots & \ddots & \vdots \\ \frac{\partial H_z^{(N)}}{\partial m_{x_i}} & \frac{\partial H_z^{(N)}}{\partial m_{y_i}} & \frac{\partial H_z^{(N)}}{\partial m_{z_i}} \end{pmatrix}. \tag{19b}$$

The various derivatives are given by:

$$\frac{\partial H_z}{\partial X} = -\frac{15XZ(\bar{R}\cdot\bar{m})}{R^7} + \frac{3Xm_z + 3Zm_x}{R^5}, \tag{20a}$$

$$\frac{\partial H_z}{\partial Y} = -\frac{15YZ(\bar{R}\cdot\bar{m})}{R^7} + \frac{3Ym_z + 3Zm_y}{R^5}, \tag{20b}$$

$$\frac{\partial H_z}{\partial Z} = -\frac{15Z^2(\bar{R}\cdot\bar{m})}{R^7} + \frac{6Zm_z}{R^5} + \frac{3(\bar{R}\cdot\bar{m})}{R^5}, \tag{20c}$$

$$\frac{\partial H_z}{\partial m_x} = \frac{3XZ}{R^5}, \tag{20d}$$

$$\frac{\partial H_z}{\partial m_y} = \frac{3YZ}{R^5}, \tag{20e}$$

$$\frac{\partial H_z}{\partial m_z} = \frac{3Z^2}{R^5} - \frac{1}{R^3}. \tag{20f}$$

Bistatic case: Using all components (H_x, H_y, H_z)

If all the components of the magnetic field are to be used, the method above can be directly generalized. Defining $\bar{\bar{J}}_x$ and $\bar{\bar{J}}_y$ in the same way as in Eq. (19a), the Jacobian and the right-hand side term become

$$\bar{\bar{J}} = \begin{bmatrix} \bar{\bar{J}}_x \\ \bar{\bar{J}}_y \\ \bar{\bar{J}}_z \end{bmatrix}, \qquad \bar{H}^{mea} - \bar{H}^{comp} = \begin{bmatrix} \bar{H}_x^{mea} - \bar{H}_x^{comp} \\ \bar{H}_y^{mea} - \bar{H}_y^{comp} \\ \bar{H}_z^{mea} - \bar{H}_z^{comp} \end{bmatrix} \tag{21}$$

where the vectors over $\bar{H}_x$, $\bar{H}_y$, $\bar{H}_z$ denote measurements over multiple grid points.

Monostatic case with a diagonal $\bar{\bar{M}}$

In the monostatic case, we suppose that the object is aligned with the principal axis of the sensor so that the polarizability tensor $\bar{\bar{M}}$ is diagonal in the $(\hat{x},\hat{y},\hat{z})$ coordinate system. From Eq. (16), we therefore write:

$$\bar{m} = \hat{x}M_x H_x^{pr} + \hat{y}M_y H_y^{pr} + \hat{z}M_z H_z^{pr}. \tag{22}$$

The magnetic field is therefore given by

$$\bar{H} = \frac{1}{R^3}\left[\frac{3Z(\bar{R}\cdot\bar{m})}{R^2} - M_z H_z^{pr}\right] = \frac{1}{R^3}\left[\frac{3Z(XM_x H_x^{pr} + YM_y H_y^{pr} + ZM_z H_z^{pr})}{R^2} - M_z H_z^{pr}\right]. \tag{23}$$

The Jacobian is calculated like in the bistatic case, with the various derivatives given by

$$\frac{\partial H_z}{\partial X} = -\frac{15XZ(\bar{R}\cdot\bar{m})}{R^7} + \frac{3Xm_z + 3Zm_x}{R^5} - \frac{\partial_x m_z}{R^3} + \frac{3Z(\bar{R}\cdot\partial_x\bar{m})}{R^5}, \tag{24a}$$

$$\frac{\partial H_z}{\partial Y} = -\frac{15YZ(\bar{R}\cdot\bar{m})}{R^7} + \frac{3Ym_z + 3Zm_y}{R^5} - \frac{\partial_y m_z}{R^3} + \frac{3Z(\bar{R}\cdot\partial_y\bar{m})}{R^5}, \tag{24b}$$

$$\frac{\partial H_z}{\partial Z} = -\frac{15Z^2(\bar{R}\cdot\bar{m})}{R^7} + \frac{6Zm_z}{R^5} - \frac{\partial_z m_z}{R^3} + \frac{3Z(\bar{R}\cdot\partial_z\bar{m})}{R^5} + \frac{3(\bar{R}\cdot\bar{m})}{R^5}, \tag{24c}$$

$$\frac{\partial H_z}{\partial M_x} = \frac{3XZ}{R^5}H_x^{pr}, \tag{24d}$$

$$\frac{\partial H_z}{\partial M_y} = \frac{3YZ}{R^5}H_y^{pr}, \tag{24e}$$

$$\frac{\partial H_z}{\partial M_z} = \frac{3Z^2}{R^5}H_z^{pr} - \frac{H_z^{pr}}{R^3}. \tag{24f}$$

where

$$m_\eta = M_\eta H_\eta^{pr},\ \eta = x,y,z, \tag{25a}$$

$$\partial_x\bar{m} = \hat{x}M_x\partial_x H_x^{pr} + \hat{y}M_y\partial_x H_y^{pr} + \hat{z}M_z\partial_x H_z^{pr}. \tag{25b}$$

The previous equations can be directly used to build the Jacobian similar to Eqs. (19b), where the derivatives with respect to $\bar{m}$ are replaced by derivatives with respect to $\bar{\bar{M}} = \hat{x}M_x + \hat{y}M_y + \hat{z}M_z$. The generalization to the other components of the magnetic field is straightforward.

2.2.3 Results

The iterative method is implemented based on Eq. (17). The maximum number of iterations is set to 1000 (or 500, see below), but the process is stopped if one of the following condition applies:

(*i*) The inverse condition number of $\bar{\bar{J}}^T\cdot\bar{\bar{J}}$ is lower than 10^{-10}.

(*ii*) The ten previous incremental values in position $\Delta\bar{R}$ and in momentum $\Delta\bar{m}$ are smaller than 0.1 cm and 0.1, respectively. More precisely: at each iteration, the sum of increments is computed as $dr = |dx_1| + |dy_1| + \ldots + |dz_2|$ and $dm = |dm_{x1}| + \ldots + |dm_{z2}|$ and stored for the last 10 iterations. If all 10 values of dr and dm are smaller than the threshold, it is decided that the algorithm has reached convergence.

The iterative algorithm starts by making a random guess for $(\bar{R}_1,\bar{m}_1)$ and $(\bar{R}_2,\bar{m}_2)$. The bounds for the random intervals of each components are as follows: the lateral positions (x and y components)

are supposed to be within −50 cm and +50 cm, the depths (z components) are supposed to be within −20 cm and −50 cm, the momenta are supposed to be between −3 and +3. The overall process is repeated 1000 times (when only H_z is used) and 500 times (when H_x, H_y, H_z are used). The results are either directly averaged, or "bin averaged". In the latter case, bins of 1 cm (for the position) or 0.1 (for the momentum) are defined, and the average is weighted by the number of occurrences in each bin.
The algorithm is run on six cases corresponding to:

Case 1: the reference case where two dipoles are somewhat close to each other, offset on the measurement grid, and of different orientations.

Case 2: a variation of case 1 where the deepest dipole is buried much deeper.

Case 3: a variation of case 1 where the shallowest dipole has its momentum drastically reduced. This could correspond to a piece of clutter closer to the sensor than the main object.

Case 4: same as case 1 but the two objects are centered on the measurement grid. The measured magnetic field therefore presents less amplitude variations over the grid.

Case 5: same as case 2 but centered over the grid.

Case 6: same as case 3 but centered over the grid.

The results are summarized in Tabs. 4 and 5 for the case when H_z only is used, and in Tabs. 6 and 7 for the case when (H_x, H_y, H_z) are used. Results are also represented graphically in Figs. 7-12. The following comments can be drawn:

- The bin average usually performs better than the direct average.
- The depth estimation is rather robust to noise.
- Paradoxically, the estimates of the centered cases are often worse than those of the offset cases.
- It is not totally clear that using the full magnetic field (H_x, H_y, H_z) yields better estimates than using only H_z. For example, the cases where one object is deeply buried are much better predicted by using H_z only. This might be due to the specific dipole moments chosen, and deserves further investigation.
- Another poor estimation corresponds to the situation where the shallowest object has a very small dipole moment, somewhat analogous to a cluttered configuration. Here again using H_z only yields better estimates than using (H_x, H_y, H_z), and the estimations rapidly degrade with increasing noise.

Noise	$\bar{R}_1$ [cm]			$\bar{R}_2$ [cm]			$\bar{m}_1$			$\bar{m}_2$		
	x_1	y_1	z_1	x_2	y_2	z_2	m_{x_1}	m_{y_1}	m_{z_1}	m_{x_2}	m_{y_2}	m_{z_2}
Case 1	**33**	**14**	**-28**	**13**	**12**	**-35**	**0**	**2**	**1**	**3**	**0**	**1**
0%	32.9	14.1	-28.0	13.0	11.8	-34.9	0.0	2.0	1.0	3.0	0.0	1.0
1%	32.9	14.0	-28.0	12.9	11.8	-34.7	0.0	2.0	1.0	3.0	0.0	1.0
2%	32.9	14.0	-28.0	12.7	11.4	-34.4	0.0	2.0	1.0	3.0	-0.0	1.0
5%	32.4	14.4	-28.6	9.7	11.5	-35.6	0.1	2.0	1.4	2.5	-0.0	0.6
10%	30.5	15.8	-29.5	2.4	6.9	-31.9	0.6	1.8	2.0	1.4	0.0	0.2
Case 2	**33**	**14**	**-28**	**13**	**12**	**-55**	**0**	**2**	**1**	**3**	**0**	**1**
0%	33.0	14.0	-28.0	12.9	12.1	-54.7	0.0	2.0	1.0	3.0	-0.0	1.0
1%	33.0	14.0	-28.0	13.1	11.9	-54.7	0.0	2.0	1.0	3.0	-0.0	1.0
2%	33.0	14.0	-28.0	13.1	11.6	-53.8	0.0	2.0	1.0	2.9	-0.0	1.0
5%	32.7	14.0	-28.2	11.6	8.6	-48.0	0.1	2.0	1.1	2.4	-0.1	0.9
10%	32.3	15.0	-28.6	4.5	3.3	-35.1	0.2	2.0	1.3	1.5	-0.0	0.6
Case 3	**33**	**14**	**-28**	**13**	**12**	**-35**	**0**	**0.2**	**0.1**	**3**	**0**	**1**
0%	26.0	13.0	-30.3	12.2	13.2	-34.6	0.7	-0.7	-0.3	2.3	0.9	1.4
1%	25.4	13.6	-30.0	10.2	11.9	-33.7	0.9	-0.5	-0.1	2.2	0.7	1.2
2%	22.1	14.3	-31.0	3.9	8.7	-30.0	1.5	-0.2	0.4	1.6	0.4	0.7
5%	18.1	14.2	-32.8	-0.2	2.5	-23.5	2.2	-0.1	0.8	0.8	0.2	0.4
10%	17.1	14.0	-33.4	-3.2	-1.9	-21.1	2.4	-0.0	0.9	0.6	0.2	0.3
Case 4	**10**	**1**	**-28**	**-10**	**-1**	**-35**	**0**	**2**	**1**	**3**	**0**	**1**
0%	12.6	3.6	-28.6	-6.3	1.2	-34.1	0.3	1.5	0.8	2.7	0.2	1.0
1%	12.7	3.6	-28.6	-6.3	1.4	-34.4	0.3	1.5	0.8	2.7	0.2	1.0
2%	12.5	3.5	-28.5	-6.5	1.3	-34.2	0.3	1.5	0.8	2.7	0.1	1.0
5%	12.3	3.5	-28.6	-5.8	1.5	-33.5	0.4	1.5	0.9	2.6	0.1	1.0
10%	10.1	4.9	-29.3	-3.8	0.5	-29.1	1.0	1.3	1.4	1.8	0.2	0.7
Case 5	**10**	**1**	**-28**	**-10**	**-1**	**-55**	**0**	**2**	**1**	**3**	**0**	**1**
0%	12.4	3.1	-28.4	-6.7	1.0	-51.1	0.2	1.5	0.8	2.8	0.1	1.0
1%	12.1	2.9	-28.6	-5.8	0.9	-50.1	0.2	1.6	0.9	2.7	0.1	0.9
2%	11.4	2.3	-28.6	-5.8	0.0	-50.5	0.2	1.7	1.0	2.6	0.0	0.9
5%	11.2	2.4	-28.7	-4.0	-0.4	-43.7	0.3	1.7	1.1	2.1	0.0	0.9
10%	10.7	3.4	-29.5	-2.8	-0.3	-30.4	0.4	1.7	1.3	1.2	0.1	0.6
Case 6	**10**	**1**	**-28**	**-10**	**-1**	**-35**	**0**	**0.2**	**0.1**	**3**	**0**	**1**
0%	8.4	2.9	-28.9	-8.1	1.6	-34.6	0.5	-0.2	-0.0	2.5	0.4	1.2
1%	6.1	1.6	-29.4	-10.0	0.6	-34.5	0.5	-0.2	-0.0	2.5	0.4	1.1
2%	5.0	2.1	-29.5	-8.9	0.1	-33.5	0.8	-0.0	0.2	2.2	0.2	0.9
5%	-1.0	1.8	-32.0	-3.9	0.2	-24.7	1.8	0.1	0.7	1.2	0.1	0.4
10%	-2.7	1.6	-32.2	-2.8	-0.8	-22.4	2.0	0.0	0.8	0.9	0.1	0.3

Table 4: Estimation of $(\bar{R}_1, \bar{m}_1)$ and $(\bar{R}_2, \bar{m}_2)$ when only H_z is used. Values correspond to direct averages.

Noise	$\bar{R}_1$ [cm]			$\bar{R}_2$ [cm]			$\bar{m}_1$			$\bar{m}_2$		
	x_1	y_1	z_1	x_2	y_2	z_2	m_{x_1}	m_{y_1}	m_{z_1}	m_{x_2}	m_{y_2}	m_{z_2}
Case 1	**33**	**14**	**-28**	**13**	**12**	**-35**	**0**	**2**	**1**	**3**	**0**	**1**
0%	33.0	14.0	-28.0	13.0	12.0	-35.0	-0.0	2.0	1.0	3.0	-0.0	1.0
1%	33.0	14.0	-28.0	13.0	12.0	-35.0	-0.0	2.0	1.0	3.0	0.0	1.0
2%	33.0	13.9	-28.0	13.1	12.1	-34.9	-0.0	2.0	1.0	3.0	0.0	1.0
5%	32.6	14.0	-28.4	13.0	11.9	-34.7	-0.0	1.8	1.1	2.8	0.0	0.9
10%	31.2	15.6	-29.9	9.7	10.9	-32.5	0.1	1.7	1.7	1.2	0.0	0.3
Case 2	**33**	**14**	**-28**	**13**	**12**	**-55**	**0**	**2**	**1**	**3**	**0**	**1**
0%	33.0	14.0	-28.0	13.0	12.0	-55.0	0.0	2.0	1.0	3.0	-0.0	1.0
1%	33.0	14.0	-28.0	13.1	12.0	-54.8	-0.0	2.0	1.0	3.0	0.0	1.0
2%	33.0	14.0	-28.0	13.1	12.0	-54.2	0.0	2.0	1.0	2.9	0.0	1.0
5%	32.9	14.0	-28.3	13.0	10.0	-49.8	0.0	2.0	1.0	2.5	-0.0	0.9
10%	32.6	14.7	-28.8	10.1	8.0	-33.7	0.1	2.0	1.3	0.5	-0.0	0.2
Case 3	**33**	**14**	**-28**	**13**	**12**	**-35**	**0**	**0.2**	**0.1**	**3**	**0**	**1**
0%	28.0	13.6	-29.4	12.4	12.9	-34.9	0.6	-0.6	-0.2	2.4	0.8	1.3
1%	23.4	14.9	-30.1	12.7	12.7	-34.9	0.2	0.1	0.1	2.7	0.1	1.0
2%	16.6	14.4	-33.3	11.8	12.5	-34.2	1.2	0.1	0.5	1.3	0.1	0.6
5%	14.6	14.0	-34.5	7.1	9.9	-25.3	2.6	0.1	1.0	0.2	0.0	0.1
10%	14.5	13.9	-34.3	3.1	5.9	-20.9	2.7	0.1	1.0	0.1	0.0	0.1
Case 4	**10**	**1**	**-28**	**-10**	**-1**	**-35**	**0**	**2**	**1**	**3**	**0**	**1**
0%	10.2	1.3	-28.0	-9.6	-0.6	-35.0	0.0	2.0	1.0	3.0	0.0	1.0
1%	10.3	1.3	-28.1	-9.5	-0.4	-34.9	0.0	1.8	1.0	2.9	0.0	1.0
2%	10.4	1.3	-28.1	-9.2	-0.0	-34.8	0.0	1.7	1.0	2.9	0.0	1.0
5%	11.1	1.8	-28.3	-7.8	1.5	-34.5	0.1	1.4	0.8	2.7	0.1	1.0
10%	10.0	3.8	-29.6	-5.0	2.9	-32.9	0.4	1.1	1.0	1.4	0.1	0.7
Case 5	**10**	**1**	**-28**	**-10**	**-1**	**-55**	**0**	**2**	**1**	**3**	**0**	**1**
0%	10.2	1.2	-28.0	-9.7	-0.7	-54.3	0.0	2.0	1.0	3.0	0.0	1.0
1%	10.2	1.2	-28.1	-8.8	0.1	-51.9	0.0	1.9	1.0	2.9	0.0	1.0
2%	10.2	1.1	-28.1	-8.1	-0.3	-50.7	0.0	1.9	1.0	2.8	0.1	1.0
5%	10.3	1.1	-28.5	-4.4	0.5	-43.7	0.0	1.8	0.9	2.2	0.1	1.0
10%	9.7	2.5	-29.5	-2.3	2.0	-26.7	0.2	1.8	1.3	0.4	0.0	0.2
Case 6	**10**	**1**	**-28**	**-10**	**-1**	**-35**	**0**	**0.2**	**0.1**	**3**	**0**	**1**
0%	8.6	1.3	-28.2	-10.2	-0.4	-34.9	0.2	0.0	0.0	2.8	0.2	1.0
1%	6.2	1.5	-28.8	-10.1	-0.7	-34.9	0.0	0.2	0.1	3.0	0.0	1.0
2%	2.7	1.5	-30.7	-10.0	-0.7	-34.8	0.1	0.1	0.1	2.7	0.0	1.0
5%	-8.0	0.8	-34.2	-9.0	-0.3	-28.2	1.8	0.1	0.8	0.4	0.0	0.1
10%	-8.0	0.8	-34.0	-7.4	-0.7	-22.3	2.1	0.1	0.9	0.2	0.0	0.1

Table 5: Estimation of $(\bar{R}_1, \bar{m}_1)$ and $(\bar{R}_2, \bar{m}_2)$ when only H_z is used. Values correspond to bin averages.

Noise	$\bar{R}_1$ [cm]			$\bar{R}_2$ [cm]			$\bar{m}_1$			$\bar{m}_2$		
	x_1	y_1	z_1	x_2	y_2	z_2	m_{x_1}	m_{y_1}	m_{z_1}	m_{x_2}	m_{y_2}	m_{z_2}
Case 1	**33**	**14**	**-28**	**13**	**12**	**-35**	**0**	**2**	**1**	**3**	**0**	**1**
0%	33.0	14.0	-28.0	13.0	12.0	-35.0	-0.0	2.0	1.0	3.0	-0.0	1.0
1%	33.0	14.1	-28.0	13.0	12.1	-34.9	0.0	2.0	1.0	3.0	0.0	1.0
2%	32.9	14.1	-28.0	13.0	11.9	-34.9	0.0	2.0	1.0	3.0	-0.0	1.0
5%	32.6	14.0	-28.1	12.7	10.5	-34.0	0.1	2.1	1.0	2.9	-0.1	1.0
10%	31.0	15.1	-29.0	6.0	8.1	-33.0	0.5	2.0	1.6	2.1	-0.0	0.5
Case 2	**33**	**14**	**-28**	**13**	**12**	**-55**	**0**	**2**	**1**	**3**	**0**	**1**
0%	33.0	14.0	-28.0	13.0	12.0	-55.0	0.0	2.0	1.0	3.0	-0.0	1.0
1%	33.0	14.0	-28.0	12.9	11.9	-54.9	0.0	2.0	1.0	3.0	-0.0	1.0
2%	33.0	14.0	-28.0	13.1	11.8	-55.0	0.0	2.0	1.0	3.0	-0.0	1.0
5%	32.9	14.0	-28.2	13.5	10.2	-52.1	0.1	2.0	1.1	2.7	-0.1	0.9
10%	32.4	14.4	-28.5	7.9	7.3	-40.9	0.3	2.0	1.3	1.9	-0.1	0.7
Case 3	**33**	**14**	**-28**	**13**	**12**	**-35**	**0**	**0.2**	**0.1**	**3**	**0**	**1**
0%	26.0	12.4	-30.7	12.9	13.0	-35.4	0.4	-0.4	-0.2	2.6	0.7	1.4
1%	26.6	13.7	-30.1	10.6	10.9	-34.3	0.7	-0.3	0.0	2.4	0.5	1.1
2%	23.8	14.1	-30.8	7.2	9.6	-32.4	1.1	-0.3	0.2	1.9	0.5	0.9
5%	20.4	14.2	-32.0	2.8	3.5	-25.8	1.8	0.0	0.7	1.2	0.2	0.5
10%	18.0	13.8	-33.3	-0.8	1.9	-22.1	2.2	0.0	0.8	0.8	0.2	0.3
Case 4	**10**	**1**	**-28**	**-10**	**-1**	**-35**	**0**	**2**	**1**	**3**	**0**	**1**
0%	12.8	3.0	-28.4	-6.1	1.3	-35.4	0.1	1.6	0.8	2.9	0.1	1.1
1%	12.8	3.0	-28.4	-6.0	1.3	-35.3	0.1	1.6	0.8	2.9	0.1	1.1
2%	12.7	3.0	-28.4	-5.9	1.2	-35.3	0.1	1.6	0.8	2.9	0.1	1.1
5%	12.5	2.9	-28.5	-5.8	1.2	-35.0	0.2	1.7	0.9	2.8	0.0	1.0
10%	11.4	3.4	-28.7	-4.3	0.1	-32.1	0.5	1.7	1.1	2.4	-0.0	0.9
Case 5	**10**	**1**	**-28**	**-10**	**-1**	**-55**	**0**	**2**	**1**	**3**	**0**	**1**
0%	12.1	2.6	-28.4	-6.9	0.9	-52.7	0.1	1.7	0.9	2.9	0.1	1.0
1%	12.1	2.6	-28.4	-6.7	0.8	-52.6	0.1	1.7	0.9	2.9	0.1	1.0
2%	11.4	1.9	-28.5	-6.7	-0.2	-52.4	0.1	1.9	1.1	2.8	-0.0	0.9
5%	10.9	1.8	-28.5	-5.9	-0.8	-49.4	0.2	1.9	1.1	2.6	-0.0	0.9
10%	10.6	2.2	-28.8	-5.3	0.2	-38.8	0.2	1.9	1.2	1.9	-0.0	0.8
Case 6	**10**	**1**	**-28**	**-10**	**-1**	**-35**	**0**	**0.2**	**0.1**	**3**	**0**	**1**
0%	8.0	2.3	-29.0	-8.7	0.4	-36.5	0.5	0.0	0.1	2.4	0.3	1.1
1%	7.4	1.0	-30.0	-8.1	0.6	-36.2	0.3	0.1	0.1	2.7	0.3	1.1
2%	6.9	1.4	-29.5	-7.7	0.9	-35.1	0.5	0.1	0.2	2.5	0.2	1.0
5%	1.3	2.2	-31.3	-5.0	0.4	-29.0	1.5	0.2	0.8	1.4	0.1	0.4
10%	-2.1	1.6	-32.9	-1.8	-0.7	-22.7	2.1	0.3	1.0	0.9	0.0	0.2

Table 6: Estimation of $(\bar{R}_1, \bar{m}_1)$ and $(\bar{R}_2, \bar{m}_2)$ when (H_x, H_y, H_z) are used. Values correspond to direct averages.

Noise	$\bar{R}_1$ [cm]			$\bar{R}_2$ [cm]			$\bar{m}_1$			$\bar{m}_2$		
	x_1	y_1	z_1	x_2	y_2	z_2	m_{x_1}	m_{y_1}	m_{z_1}	m_{x_2}	m_{y_2}	m_{z_2}
Case 1	**33**	**14**	**-28**	**13**	**12**	**-35**	**0**	**2**	**1**	**3**	**0**	**1**
0%	33.0	14.0	-28.0	13.0	12.0	-35.0	-0.0	2.0	1.0	3.0	-0.0	1.0
1%	33.0	14,0	-28.0	13.0	12.0	-34.9	-0.0	2.0	1.0	3.0	0.0	1.0
2%	32.9	13.9	-28.0	13.1	11.8	-34.9	0.0	2.0	1.0	3.0	-0.0	1.0
5%	32.7	13.9	-28.1	13.3	11.8	-34.5	0.0	2.0	1.0	2.9	0.0	1.0
10%	31.4	14.8	-29.3	12.0	11.2	-34.1	0.1	1.8	1.3	2.0	0.0	0.7
Case 2	**33**	**14**	**-28**	**13**	**12**	**-55**	**0**	**2**	**1**	**3**	**0**	**1**
0%	33.0	14.0	-28.0	13.0	12.0	-55.0	0.0	2.0	1.0	3.0	-0.0	1.0
1%	33.0	14.0	-28.0	12.9	11.8	-54.9	0.0	2.0	1.0	3.0	-0.0	1.0
2%	33.0	14.0	-28.0	13.1	12.2	-54.8	0.0	2.0	1.0	3.0	0.0	1.0
5%	33.0	13.9	-28.0	13.2	10.9	-53.0	0.0	2.0	1.0	2.8	-0.0	1.0
10%	32.7	14.2	-28.6	11.5	9.5	-44.5	0.1	2.0	1.1	1.4	-0.0	0.5
Case 3	**33**	**14**	**-28**	**13**	**12**	**-35**	**0**	**0.2**	**0.1**	**3**	**0**	**1**
0%	28.3	12.4	-29.9	12.9	12.5	-35.0	0.2	-0.3	-0.2	2.8	0.6	1.3
1%	25.7	14.6	-29.5	12.8	12.5	-35.0	0.2	0.1	0.1	2.9	0.1	1.0
2%	19.6	14.5	-32.1	12.4	12.5	-34.9	0.6	0.1	0.3	2.2	0.1	0.9
5%	15.8	13.8	-34.3	10.6	10.8	-31.8	1.9	0.1	0.9	0.6	0.0	0.2
10%	14.9	13.8	-34.4	6.2	8.7	-26.0	2.4	0.1	1.0	0.2	0.0	0.1
Case 4	**10**	**1**	**-28**	**-10**	**-1**	**-35**	**0**	**2**	**1**	**3**	**0**	**1**
0%	10.3	1.2	-28.0	-9.6	-0.7	-35.0	0.0	2.0	1.0	3.0	0.0	1.0
1%	10.4	1.2	-28.0	-9.5	-0.6	-35.0	0.0	1.9	1.0	3.0	0.0	1.0
2%	10.6	1.2	-28.1	-9.3	-0.4	-35.1	0.0	1.9	0.9	3.0	0.0	1.0
5%	11.2	1.4	-28.2	-8.5	0.1	-34.7	0.0	1.7	0.9	2.9	0.0	1.1
10%	11.6	2.2	-28.9	-6.4	1.3	-34.2	0.1	1.4	0.8	2.5	0.1	0.9
Case 5	**10**	**1**	**-28**	**-10**	**-1**	**-55**	**0**	**2**	**1**	**3**	**0**	**1**
0%	10.2	1.1	-28.0	-9.8	-0.8	-54.7	0.0	2.0	1.0	3.0	0.0	1.0
1%	10.3	1.1	-28.0	-9.5	-0.5	-54.0	0.0	2.0	1.0	3.0	0.0	1.0
2%	10.2	1.0	-28.1	-9.1	-0.6	-53.6	0.0	2.0	1.0	3.0	0.0	1.0
5%	10.2	1.0	-28.1	-8.5	-0.3	-51.1	0.0	2.0	1.0	2.8	0.0	1.1
10%	9.7	1.4	-28.9	-5.6	-0.5	-41.2	0.1	2.0	1.0	1.2	0.0	0.5
Case 6	**10**	**1**	**-28**	**-10**	**-1**	**-35**	**0**	**0.2**	**0.1**	**3**	**0**	**1**
0%	8.6	1.4	-28.3	-10.4	-0.4	-34.9	0.2	-0.0	0.0	2.8	0.2	1.1
1%	8.3	1.1	-28.6	-9.9	-0.8	-35.1	0.0	0.2	0.1	3.0	0.0	1.0
2%	6.5	1.4	-29.4	-9.8	-0.7	-35.0	0.0	0.2	0.1	2.9	0.0	1.0
5%	-6.5	1.1	-33.9	-8.9	-0.3	-32.6	1.3	0.1	0.8	0.7	0.0	0.3
10%	-8.2	0.8	-34.5	-4.9	0.0	-20.9	2.3	0.2	1.1	0.1	0.0	0.0

Table 7: Estimation of $(\bar{R}_1, \bar{m}_1)$ and $(\bar{R}_2, \bar{m}_2)$ when (H_x, H_y, H_z) are used. Values correspond to bin averages.

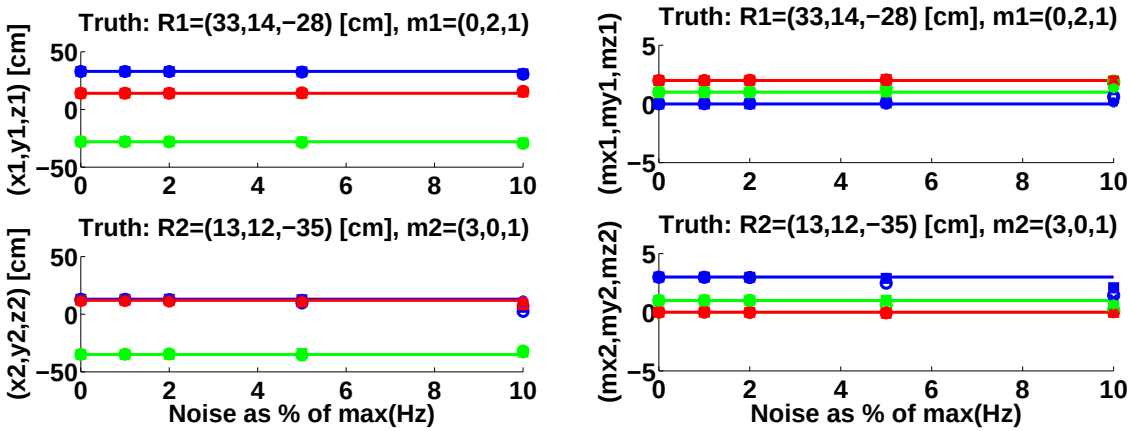

(a) Estimation in position. (b) Estimation in momentum.

Figure 7: Case 1: estimations of $(\bar{R}_1, \bar{m}_1)$ and $(\bar{R}_2, \bar{m}_2)$ in the case of direct averages and bin averages, when both H_z and (H_x, H_y, H_z) are used. The cases correspond to Tabs. 4-7. Legend: '$\circ$' for H_z straight average; '$\times$' for H_z bin average; '$\square$' for (H_x, H_y, H_z) straight average; '$*$' for (H_x, H_y, H_z) bin average. Solid lines correspond to true values: $\hat{x}$ component is in blue, $\hat{y}$ component in red, $\hat{z}$ component in green.

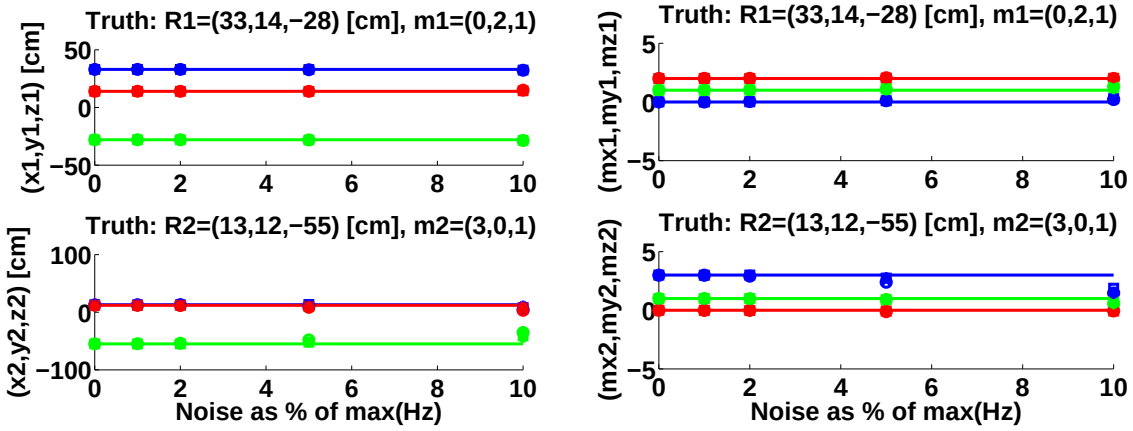

(a) Estimation in position. (b) Estimation in momentum.

Figure 8: Case 2: estimations of $(\bar{R}_1, \bar{m}_1)$ and $(\bar{R}_2, \bar{m}_2)$ in the case of direct averages and bin averages, when both H_z and (H_x, H_y, H_z) are used. The cases correspond to Tabs. 4-7. See Fig. 7 for details on the legend.

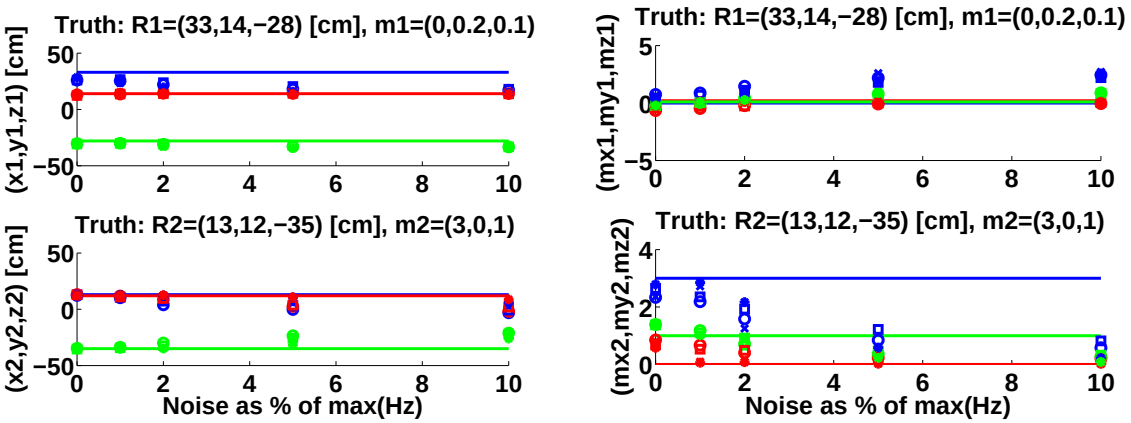

(a) Estimation in position. (b) Estimation in momentum.

Figure 9: Case 3: estimations of $(\bar{R}_1, \bar{m}_1)$ and $(\bar{R}_2, \bar{m}_2)$ in the case of direct averages and bin averages, when both H_z and (H_x, H_y, H_z) are used. The cases correspond to Tabs. 4-7. See Fig. 7 for details on the legend.

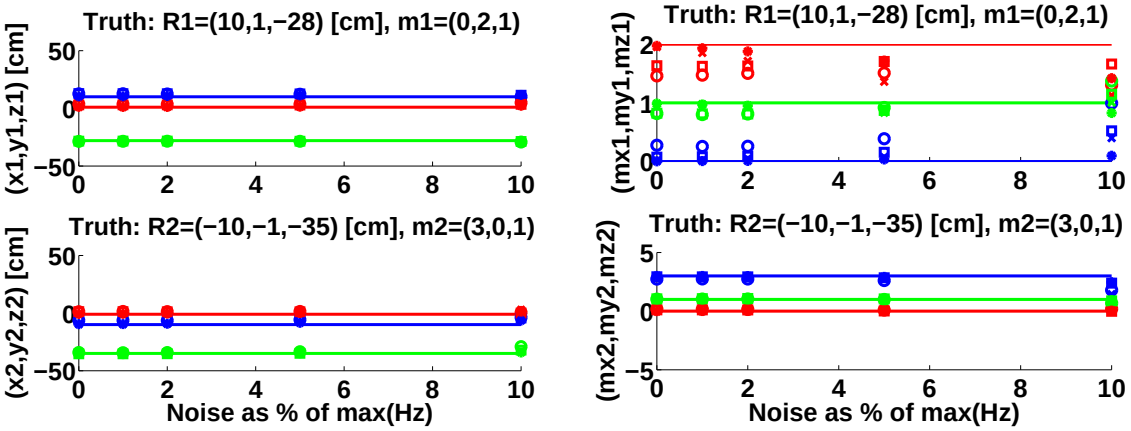

(a) Estimation in position. (b) Estimation in momentum.

Figure 10: Case 4: estimations of $(\bar{R}_1, \bar{m}_1)$ and $(\bar{R}_2, \bar{m}_2)$ in the case of direct averages and bin averages, when both H_z and (H_x, H_y, H_z) are used. The cases correspond to Tabs. 4-7. See Fig. 7 for details on the legend.

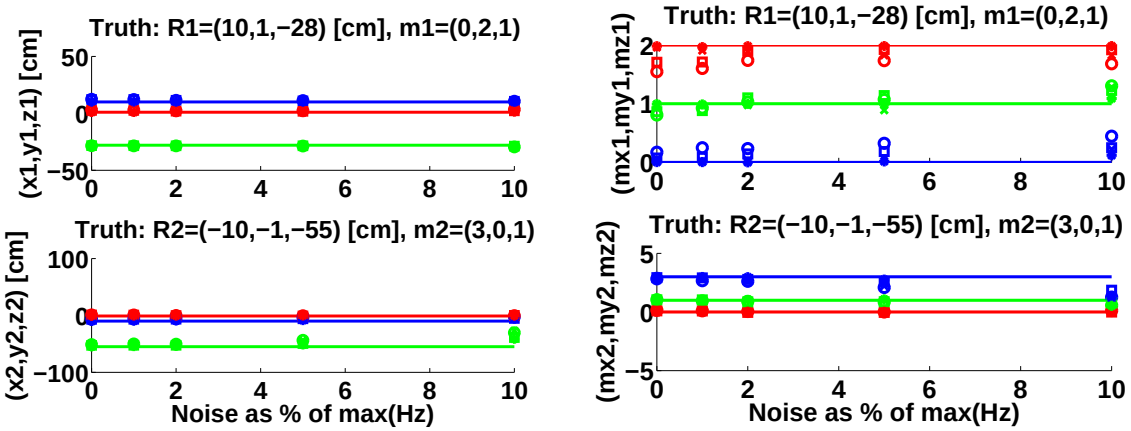

(a) Estimation in position. (b) Estimation in momentum.

Figure 11: Case 5: estimations of $(\bar{R}_1, \bar{m}_1)$ and $(\bar{R}_2, \bar{m}_2)$ in the case of direct averages and bin averages, when both H_z and (H_x, H_y, H_z) are used. The cases correspond to Tabs. 4-7. See Fig. 7 for details on the legend.

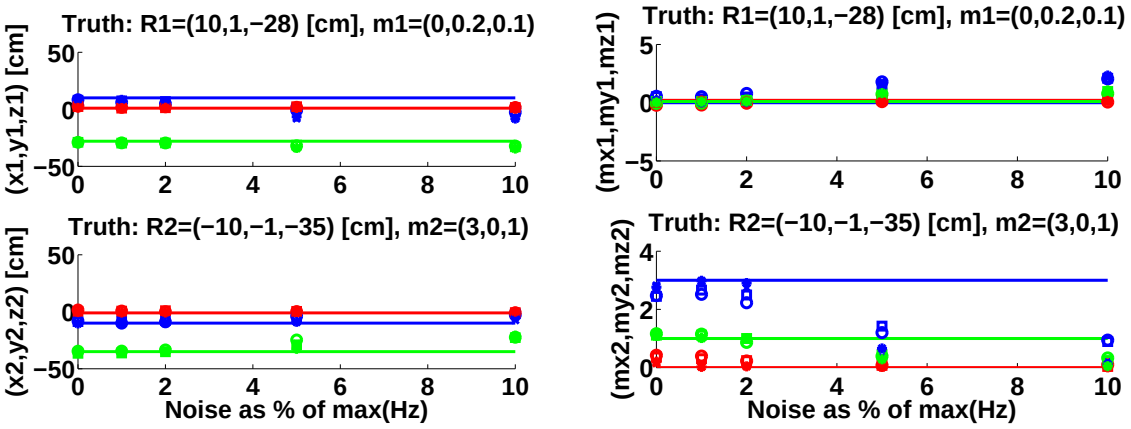

(a) Estimation in position. (b) Estimation in momentum.

Figure 12: Case 6: estimations of $(\bar{R}_1, \bar{m}_1)$ and $(\bar{R}_2, \bar{m}_2)$ in the case of direct averages and bin averages, when both H_z and (H_x, H_y, H_z) are used. The cases correspond to Tabs. 4-7. See Fig. 7 for details on the legend.

Noise	Case 1	Case 2	Case 3	Case 4	Case 5	Case 6
0%	43.8 (37.0)	42.4 (29.0)	38.8 (27.8)	48.7 (38.6)	47.6 (36.0)	43.6 (38.6)
1%	43.2 (33.0)	41.6 (27.4)	45.5 (38.8)	47.3 (40.6)	44.6 (38.8)	39.9 (36.8)
2%	40.3 (34.4)	40.6 (26.0)	47.9 (43.2)	48.3 (41.8)	45.4 (32.6)	43.7 (35.8)
5%	47.0 (29.6)	54.8 (30.0)	56.0 (44.4)	55.6 (41.2)	56.9 (31.0)	52.9 (38.6)
10%	66.0 (45.6)	64.0 (46.0)	58.1 (46.8)	64.0 (50.6)	59.1 (44.2)	55.0 (44.6)

Table 8: Percentage of divergent cases when H_z is used and when (H_x, H_y, H_z) is used (the values corresponding to the latter case are indicated in parenthesis). The case number refers to Tabs. 4-7.

A statistics in divergence rates is also presented in Table 8. It can be seen that the divergence rates drops sometimes significantly when the full vectorial magnetic field is used, as opposed to when only H_z is used. Note also that the number of diverging cases (and therefore number of false detections) depends on the threshold set for the matrix conditioning (10^{-10} here). Relaxing this condition yields less divergences and more false detection, and conversely. However, it might appear preferable to have more divergences (which can be discarded in the decision making process) for an increased probability of detection. In Table 8, the percentage of correct detections has been computed after discarding the divergent cases.

3 Conclusions and future work

Despite the analytical appeal of the $(\bar{H}, \bar{A}, \psi)$ method, its limitation to single target inversion drastically hinders its applicability in realistic situations, where UXO are often buried alongside clutter items. In order to overcome this limitation, we have proposed a different approach, more numerically involved but also of much broader applicability: the iterative Gauss-Newton method. The validation of the method has been performed here with two synthetic targets which have been properly identified, despite varying degrees of noise. The analytical computation of the Jacobian matrices contributes to the efficiency of the method and make it a good candidate for future investigation. We therefore suggest additional investigations into the Gauss-Newton algorithm in order to establish its accuracy with real sensor data, first in single target and then in multi-target configurations. In particular, the stability of the algorithm to the increasing number of targets (hence the increasing number of unknowns) should be investigated, as well as the proper formulation of the unknown vector which could include a single, a few, or all time channels.

4 Bibliography

[1] H. Braunisch, C. O. Ao, K. O'Neill, and J. A. Kong, "Magnetoquasistatic response of conducting and permeable prolate spheroid under axial excitation," *IEEE Trans. on Geosci. Remote Sens.*, vol. 39, pp. 2689–2701, December 2001.

[2] C. O. Ao, H. Braunisch, K. O'Neill, and J. A. Kong, "Quasi-magnetostatic solution for a conducting and permeable spheroid with arbitrary excitation," *IEEE Trans. on Geosci. Remote Sens.*, vol. 40, pp. 887–897, April 2002.

[3] B. E. Barrowes, K. O'Neill, T. M. Grzegorczyk, X. Chen, and J. A. Kong, "Broadband analytical magnetoquasistatic electromagnetic induction solution for a conducting and permeable spheroid," *IEEE Trans. on Geosci. Remote Sens.*, vol. 42, pp. 2479–2489, November 2004.

[4] Y. Zhang, L. Collins, H. Yu, C. Baum, and L. Carin, "Sensing of unexploded ordnance with magnetometer sensing of unexploded ordnance with magnetometer," *IEEE Trans. on Geosci. Remote Sens.*, vol. 41, pp. 1005–1015, May 2003.

[5] T. H. Bell, B. J. Barrow, and J. T. Miller, "Subsurface discrimination using electromagnetic induction sensors," *IEEE Trans. on Geosci. Remote Sens.*, vol. 39, pp. 1286–1293, June 2001.

[6] X. Chen, K. O'Neill, T. M. Grzegorczyk, and J. A. Kong, "Spheroidal mode approach for the characterization of metallic objects using electromagnetic induction," *IEEE Trans. on Geosci. Remote Sens.*, vol. 45, pp. 697–706, March 2007.

[7] B. Zhang, K. O'Neill, J. A. Kong, and T. M. Grzegorczyk, "Support vector machine and neural network classification of metallic objects using coefficients of the spheroidal mqs response modes," *IEEE Trans. on Geosci. Remote Sens.*, 2007. accepted for publication.

[8] T. M. Grzegorczyk, B. Zhang, J. A. Kong, B. E. Barrowes, and K. O'Neill, "Electromagnetic induction from highly permeable and conductive ellipsoids under arbitrary excitation – application to the detection of unexploded ordnances," *IEEE Trans. on Geosci. Remote Sens.*, vol. 46, pp. 1164–1176, April 2008.

[9] F. Shubitidze, D. Karkashadze, B. Barrowes, I. Shamatava, and K. O'Neill, "A new physics based approach for estimating a buried object's location, orientation and magnetic polarization from EMI data," *J. Env. and Eng, Geophys.*, vol. 13, pp. 115–130, 2008.

[10] J. D. Jackson, *Classical Electrodynamics*. Wiley, third ed., 1999.